Efficient and selective phosphate removal from wastewater using surface-modified spent bleaching earth from palm oil refineries: A zero-waste approach

by Ery S. Retnoningtyas

Submission date: 12-Feb-2025 04:28AM (UTC+0700)
Submission ID: 2586026338
File name: 6-Efficient_and_selective_phosphate.pdf (14.64M)
Word count: 11190
Character count: 57695

Journal of Water Process Engineering 58 (2024) 104906

Contents lists available at ScienceDirect

Journal of Water Process Engineering

journal homepage: www.elsevier.com/locate/jwpe

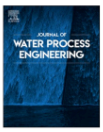

Efficient and selective phosphate removal from wastewater using surface-modified spent bleaching earth from palm oil refineries: A zero-waste approach

Putri Dwi Retno Asmoro [a], Maria Yuliana [a,b,c,*], Felycia Edi Soetaredjo [b,c], Suryadi Ismadji [b,c], Masahiro Muraoka [d], Shintaro Kawano [e], Motohiro Shizuma [e], Grandprix Thomryes Marth Kadja [f,g,h], Christian Julius Wijaya [b,c], Shella Permatasari Santoso [a,b,c], Ery Susiany Retnoningtyas [a,b]

[a] Chemical Engineering Master Program, Widya Mandala Surabaya Catholic University, Kalijudan 37, Surabaya 60114, Indonesia
[b] Department of Chemical Engineering, Widya Mandala Surabaya Catholic University, Kalijudan 37, Surabaya 60114, Indonesia
[c] Collaborative Research Center for Zero Waste and Sustainability, Kalijudan 37, Surabaya 60114, Indonesia
[d] Department of Applied Chemistry, Faculty of Engineering, Osaka Institute of Technology (OIT), 5-16-1 Ohmiya, Asahi-ku, Osaka 535-8585, Japan
[e] Osaka Research Institute of Industrial Science and Technology (ORIST), 1-6-50 Morinomiya, Joto-ku, Osaka 536-8553, Japan
[f] Division of Inorganic and Physical Chemistry, Faculty of Mathematics and Natural Sciences, Institut Teknologi Bandung, Ganesha 10, Bandung 40132, Indonesia
[g] Center for Catalysis and Reaction Engineering, Institut Teknologi Bandung, Ganesha 10, Bandung 40132, Indonesia
[h] Research Center for Nanosciences and Nanotechnology, Institut Teknologi Bandung, Ganesha 10, Bandung 40132, Indonesia

ARTICLE INFO

Editor: Sadao Araki

Keywords:
Waste-based adsorbent
Phosphate removal
Mechanism study
Selectivity study
Zero-waste approach

ABSTRACT

This research employs a zero-waste approach by utilizing the surfactant-modified spent bleaching earth (SBE) waste from palm oil refineries for phosphate removal from wastewater. Various mass ratios of n-hexane to SBE (r_{hex}), CTAB loading (m_c), and temperature (T_i) is studied to obtain the reactivated SBE with the highest phosphate removal – which is obtained at r_{hex} = 1:5, m_c = 0.5 wt%, and T_i = 30 °C and is referred to as $RSBE_m$. A 97.7 wt% removal of phosphate and 194.6 mg/g adsorption capacity can be successfully achieved at pH = 7, C_o = 150 mg/L, t = 150 min, T = 30 °C, $RSBE_m$ loading = 0.1 wt%. The kinetic, isotherm, and thermodynamic studies suggest that the phosphate uptake follows the monolayer mechanism. The studies also show that the adsorption is spontaneous, endothermic, and mainly driven by the electrostatic interaction between the cationic head of CTAB attached to the interlayer spacing of $RSBE_m$ and negative phosphate ion. $RSBE_m$ shows good reusability with the phosphate removal rate > 80 wt% until four cycles. Based on the selectivity study using the single compound and binary system approach, $RSBE_m$ also has a good selectivity towards phosphate in the presence of various co-existing anions.

1. Introduction

Phosphate is an essential nutrient for plant growth and agriculture. However, in some instances, this component is also considered a pollutant due to the possibility of accumulating toxic contaminants [1], impacting the environment and health, e.g., heart and kidney failure [2]. Excessive phosphate emission leads to accelerated eutrophication in aquatic ecosystems leading to algae blooms, water quality degradation, and oxygen depletion. In light of eutrophication, the European Union considers that the limit for total phosphate concentration ranging from no risk to risk of eutrophication in lakes is <10 μg/L to >100 μg/L. Meanwhile, for rivers, the total phosphate concentration below 0.07 μg/L is considered good quality water [3].

Sundry processes have been developed to remove phosphate to treat water contamination, e.g., biological aeration, membrane separation, and adsorption. Of the available methods, adsorption is preferable due to its simplicity, selectivity, wide concentration range, high adsorption capacity in removing various contaminants, and relatively low cost, suitable for phosphate removal [4]. Multiple studies on phosphate removal have already been reported; Angkawijaya et al. (2020) evaluate

* Corresponding author at: Chemical Engineering Master Program, Widya Mandala Surabaya Catholic University, Kalijudan 37, Surabaya 60114, Indonesia.
E-mail address: mariayuliana@ukwms.ac.id (M. Yuliana).

https://doi.org/10.1016/j.jwpe.2024.104906
Received 14 December 2023; Received in revised form 20 January 2024; Accepted 24 January 2024
2214-7144/© 2024 Elsevier Ltd. All rights reserved.

the phosphate removal onto organo-bentonite (OrB) and acid-activated bentonite (AAB), where (1) pH slightly affects the phosphate adsorption to both OrB and AAB, (2) the adsorption model shows a good fit with Langmuir model, and (3) the rapid phosphate removal at the beginning implies that the adsorption is electrostatic force-driven and promoted by physical adsorption [5]. The respective adsorption capacities are 131.7 and 97.6 mg/g (323*K*). Wang et al. (2023) reported the synthesis of La/Fe-engineered bentonite (LFB) with an adsorption capacity of 89.32 mg/g for phosphate removal [6]; meanwhile, Fu et al. (2023) presented the fabrication of carboxymethyl cellulose (CMC)/sodium alginate (SA) hydrogel beads modified with calcium carbonate ($CaCO_3$) and/or bentonite (Be) which affords an adsorption capacity of 90.31 mg P/g [7].

Spent bleaching earth (SBE) is a significant solid waste in the palm oil industry, categorized as hazardous. Based on the Indonesian Ministry of Agriculture, palm oil production is around 40 million tons per year [8], with 1.2–1.5 million tons of SBE discharged into the environment. SBE contains 20–40 % residual oil, which oxidizes rapidly and produces an offensive odor. If improperly stored or disposed of, SBE may cause fire hazards, and at the same time, its contaminants can dissolve into water, leading to severe environmental and public health issues. However, SBE finds uses as a raw material in bricks, blocks, cement production, fuel briquettes, and biodiesel production [9–12]. This material can also be an adsorbent to eliminate various product colorants. Yuliana et al. (2021) effectively employed cetyltrimethylammonium bromide (CTAB)-modified SBE for glycerol adsorption [13]. Meanwhile, Merikhy et al. (2020) also reported carbonized SBE for methylene blue adsorption with an adsorption capacity of 53.91 mg/g [14]. These investigations show that SBE has promising potential as an adsorbent material. Furthermore, Bacelo et al. (2020) stated that an adsorbent rich in iron, calcium, magnesium, and other alkaline earth metal ions is compatible and practical for phosphate adsorption because these metals have a high affinity to the targeted phosphate ion [15]. Therefore, this research seeks to explore the use of SBE, which possesses a high content of alkaline earth metal ions, as an adsorbent for phosphate removal: addressing phosphate contamination in water systems cost-effectively and, at the same time, supporting the concept of a circular economy and zero-waste act.

However, due to the limited adsorption capacity of SBE, material reactivation using cationic surfactants is employed to improve this drawback. The cationic surfactant, cetyltrimethylammonium bromide (CTAB), is selected because it has long hydrocarbon chains that promote electrostatic interactions and physical adsorption on the surface of SBE. Shao et al. (2022) studied that the positive charge of an adsorbent can be increased after surfactant modification [16]. The textural properties of the material are also observed to improve, hence, favorable to the adsorption process. Khenifi et al. (2009) reported that the cationic head of surfactant is incorporated into the interlayer area of bentonite, increasing the *d*-spacing (basal spacing) and developing a better pore structure [17].

In this study, the reactivation condition of SBE is studied at various mass ratios of n-hexane to SBE (r_{hex}), CTAB loading (m_c), and temperature (T_i). The performance of every reactivated SBE (RSBE) is investigated to obtain the RSBE giving the highest phosphate removal ($RSBE_m$). The adsorption capacity and behavior of $RSBE_m$ are examined by the isotherm, kinetic, and thermodynamic studies. Its selectivity towards phosphate is also evaluated by studying the influence of co-existing anions. Moreover, the reusability study is conducted to assess the economic benefit of the adsorbent.

2. Experimental section

2.1. Materials

SBE is collected from the local palm oil industry, PT Batara Elok Semesta Terpadu (Gresik, Indonesia). Meanwhile, n-hexane (CAS no. 110–54-3, 99 % purity), CTAB (CAS no. 57–09-0, >98 % purity), methanol (CAS no. 67–56-1, 99 %), sodium hydroxide (NaOH, CAS no. 1310-73-2, 98 % purity), sulfuric acid (H_2SO_4, CAS no. 7664-93-9, 99.9 % purity), potassium dihydrogen phosphate (KH_2PO_4, CAS no. 7778-77-0, >99 % purity) are purchased from Sigma-Aldrich (Germany). All chemicals and reagents are analytical and can be used as received.

2.2. Surfactant modification of SBE

SBE reactivation is carried out according to Yuliana et al. (2020) [13], with a slight modification. Initially, a series of n-hexane and SBE mixtures with $r_{hex} = 5$, 10, and 15 are stirred for 30 min at 45 °C and 300 rpm. The defatted SBE is collected by centrifugation and washed using methanol three times. To maximize the surface area for subsequent modification, the calcination step is conducted at 550 °C for 120 min under an aerobic atmosphere, ensuring complete combustion of residual organic matter. The surface activation is then employed by impregnating CTAB into the interlayer of SBE using $m_c = 0.5$, 0.75, 1 wt% with a reaction time of 180 min. The intercalation temperature is maintained constant at three levels, T_i = 30, 40, and 50 °C. The RSBE solids are separated using centrifugation at 4500 rpm for 10 min, repeatedly washed with water, and oven-dried at 120 °C.

2.3. The performance of RSBE on the removal of phosphate

To determine the performance of RSBE obtained at various intercalation parameters, 100 mL of KH_2PO_4 solution (with the initial phosphate concentration, C_o = 150 mg/L) and 0.1 wt% RSBE are mixed at 300 rpm, pH = 7 and adsorption temperature (T) of 30 °C. The following equation calculates the phosphate removal:

$$\text{Phosphate removal (R, wt\%)} = \frac{C_o - C_e}{C_o} \times 100 \quad (1)$$

where C_o is the initial phosphate concentration (mg/L), and C_e is the final phosphate concentration (mg/L). All phosphate concentrations in this study are determined using Shimadzu UV–Vis spectrophotometer 2600 (Shimadzu, Japan) at a wavelength (λ) of 880 nm. Meanwhile, the cation exchange capacity (CEC) of RSBE is measured following the standard method of ASTM C837-99.

2.4. The adsorption study

The kinetic study of the phosphate removal is conducted in a series of flasks, where 0.1 wt% of $RSBE_m$ is introduced to 10 mL of KH_2PO_4 solution (C_o = 150 mg/L, pH = 7) in each flask. Each flask is collected at different adsorption times (t = 10–240 min), and the loaded amount of phosphate in $RSBE_m$ is measured. The equilibrium obtained is referred to as t_{eq}. Meanwhile, the isotherm study is performed by introducing 10 mg $RSBE_m$ to 10 mL KH_2PO_4 solution at various C_o (C_o = 20–200 mg/L) and agitated with the time interval of t_{eq}. Both studies are investigated at three temperature levels (T = 30, 40, 50 °C) with three replicates for each run.

The calculation of adsorption capacity at a particular time (q_t) and equilibrium (q_e) can be done using the following equations, where C_o, C_t, and C_e are the concentration of phosphate at $t = 0$, $t = t$ and $t = t_{eq}$ (mg/L), m_a represents to the mass of $RSBE_m$ (g), and V is the volume of KH_2PO_4 solution. As previously mentioned in Subsection 2.3, all concentrations of phosphate are analyzed using a spectrophotometer at λ = 880 nm.

$$q_t = \frac{(C_0 - C_t)V}{m_a} \quad (2)$$

$$q_e = \frac{(C_0 - C_e)V}{m_a} \quad (3)$$

To illustrate the adsorption behavior, the data at equilibrium are fitted to several kinetic and isotherm models, e.g., pseudo-first-order (PFO), pseudo-second-order (PSO), Elovich, intraparticle diffusion (IPD), Langmuir, Freundlich, Sips, Redlich-Peterson, and Temkin, whose equations are summarized in Table S1. Further, the thermodynamic parameters, namely Gibbs free energy (ΔG°), enthalpy (ΔH°), and entropy (ΔS°), are computed using the obtained isotherm parameters.

2.5. The reusability study

The reusability study is employed for six identical adsorption/regeneration/desorption cycles, where the regeneration of the used $RSBE_m$ is conducted by (1) water-washing for 30 min under stirring, (2) centrifugation at 4500 rpm, (3) methanol-washing to ensure the removal of residue, and (4) overnight drying at 80 °C. All experiments are carried out in triplicates.

2.6. Characterization of $RSBE_m$

Both SBE and $RSBE_m$ are characterized for their crystallinity using X-ray diffraction (XRD) RINT2500/PC (Rigaku Corp., Tokyo, Japan), operating at 40 kV, 40 mA tube current, and 2.00°/min radiation scan speed. The monochromatic Cu Kα is used at λ = 1.54 Å. The scanning electron microscopy-energy dispersion spectroscopy (SEM-EDS) analysis is obtained using a JEOL JSM-6610LA (Jeol Ltd., Japan), with a beam current, count rate, and working voltage at 10 μm, 186/s, and 15 kV, respectively. The conductivity of both samples is provided through a fine-coat gold sputtering using JEOL JFC-1100 (Jeol Ltd., Japan) to prevent electron charging on the surface. The EDS mapping is also performed using the same instrument for carbon, oxygen, sodium, magnesium, aluminum, silica, calcium, and iron elements. Meanwhile, the FTIR spectra are obtained using Bruker-Alpha 1 (Bruker, Germany) in 500–4000 cm^{-1}. The nitrogen (N_2) adsorption-desorption analysis uses a Micromeritics ASAP 2010 sorption analyzer (Micromeritics Instrument Corporation, USA) at 77 K. The sample is degassed at 423 K for 2 h before analysis. The point of zero charge (pH_{pzc}) is analyzed using the drift method at the range of 2–12.

3. Results and discussion

3.1. The influence of intercalation variables on the RSBE performance in phosphate removal

The influence of the intercalation variables (r_{hex}, m_c, T_i) on phosphate removal is studied to evaluate the RSBE performance and determine $RSBE_m$. Fig. 1a-c presents the performance of RSBE intercalated at various conditions. As seen, there is no significant change in phosphate removal when r_{hex} is increased from r_{hex} = 1:5 to r_{hex} = 1:15 during the fabrication of RSBE; only a slight decline is observed. This reveals that higher r_{hex} negatively correlates to phosphate removal, probably due to the outright migration of SBE elements to n-hexane, further decreasing adsorption site formation in RSBE [18]. The influence of intercalation temperature (T_i) on adsorption capacity (q_e) does not exhibit a clear trend. While a slight increase in q_e is observed at T_i = 40 °C compared to T_i = 30 °C for some r_{hex} values, this is not a consistent trend across all conditions – notably, at T_i = 50 °C, a moderate decline in q_e is observed for several r_{hex} values. At one point, the high solubility of surface cations at more elevated temperatures promotes their migration to the bulk solution, drives the attachment of the cationic head of CTAB onto the interlayer to maintain the surface charge [19], and enlarges the *d*-spacing of RSBE. However, the interaction between the cationic head of CTAB and the material surface also creates a denser area loaded with hydrophobic tails of CTAB, which reduces the possibility of RSBE interacting with phosphate, thus, resulting in the stagnant performance of T_i-varied RSBE.

In terms of m_c, a correspondingly lower m_c exhibits a good adsorption performance of RSBE. This may be related to the more significant interaction between vacant sites on the RSBE surface and the cationic head of CTAB to generate a hemimicelle layer at higher surfactant concentration, which lowers the number of available active sites for phosphate adsorption. Gürses et al. (2009) also mentioned that increasing m_c generates a hydrophobic region, which is unsuitable for the adsorption processes [20]. Concluding the abovementioned results, this research sees that the higher the three intercalation parameters, the denser the interlayer spacing. This phenomenon closes the available active sites on RSBE and, as a result, decreases its ability for phosphate adsorption [19]. This aligns with cation exchange capacity (CEC)

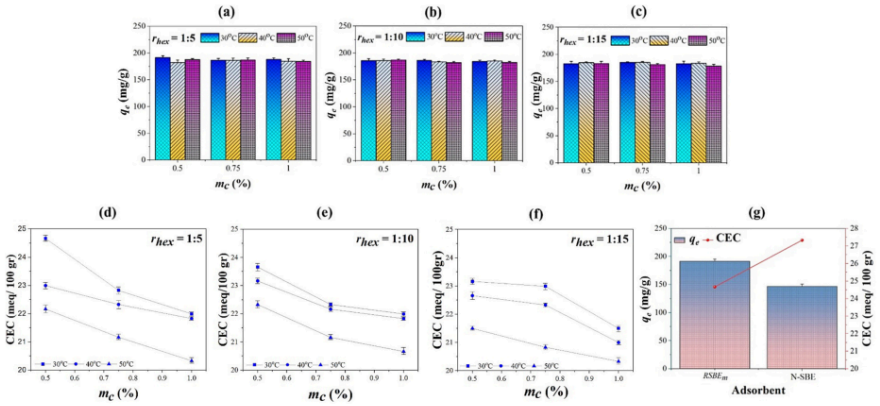

Fig. 1. The influence of intercalation variables in the fabrication of RSBE on (a–c) the adsorption capacity (adsorption condition: pH = 7, C_o = 150 mg/L, t = 150 min, T = 30 °C, $RSBE_m$ loading = 0.1 wt%) and (d–f) the CEC values (test condition: pH = 3), (g) the performance comparison between $RSBE_m$ and N-SBE.

analysis in Fig. 1d-f. CEC value is proportional to the number of cations that can be held in the material, and materials with higher CEC generally perform better in adsorbing and retaining components. Notably from the figures, the higher intercalation parameters generally correspond to decreased CEC values. While m_c and T influence CEC prominently, r_{hex} does not show a significant effect on CEC, as the value only fluctuates with little margin, if not fairly similar. Therefore, RSBE obtained at the lowest intercalation levels (r_{hex} = 1:5, m_c = 0.5 wt%, and T_i = 30 °C) with the respective adsorption capacity and phosphate removal rate of 194.6 mg/g and 97.7 wt%, is deemed as *RSBE*$_m$ for its greater performance in the phosphate removal compared with the others. Fig. 1g represents the comparative results of q_e and CEC between *RSBE*$_m$ and not-intercalated SBE (N-SBE). *RSBE*$_m$ shows greater performance than N-SBE, as *RSBE*$_m$ contains a higher number of active sites available for the adsorption process. The employed student *t*-test results in an α value of <0.05, confirming the significant difference between the performance of *RSBE*$_m$ and N-SBE in removing phosphate.

3.2. Characterization

XRD analysis of the four samples, *RSBE*$_m$, N-SBE, and their after-adsorption counterparts (*RSBEm*@P and N-SBE@P), are shown in Fig. 2. The diffraction profile resembles a pattern of SBE reported by Mana (2011) [21]. The computed crystallinity of *RSBE*$_m$ obtained using PDXL software is 70 %, with an individual crystal size of 300–600 Å. The XRD datasets are processed by Match! software with the Dicvol06 program; all samples show characteristic peaks for the montmorillonite phase (JCPDS 12–0219) at 2θ = 20.4° ($\bar{0}02$) and quartz phase (JCPDS 05–490) at 2θ = 26.8°, while according to JCPDS 71–0957, all samples reveal the orthoclase phase at 2θ = 23.6° ($\bar{1}30$), 25.5° ($\bar{1}12$), 27.8° ($\bar{0}02$), 31.4° ($\bar{0}41$), and 32.9° ($\bar{1}32$) [22]. In the case of *RSBE*$_m$, there exists an indentation at 2θ =19.6° ($\bar{0}01$), confirming an increase in *d*-spacing of intercalated layers from 2.156 Å in N-SBE to 3.234 Å in *RSBE*$_m$ (the data are presented in Table S2 – S3), which is due to the presence of CTAB [23]. Both *RSBE*$_m$ and N-SBE share similar diffraction profiles with *RSBE*$_m$@P and N-SBE@P, indicating the main structure of *RSBE*$_m$@P and N-SBE@P remains unaltered during adsorption.

Fig. 3 depicts the FTIR profiles of *RSBE*$_m$, *RSBE*$_m$@P, N-SBE, and N-SBE@P. This analysis is used to understand the mechanism of phosphate adsorption through their functional groups. All samples observe a broad peak at 3621 cm^{-1}, indicating the presence of the stretching of OH$^-$ groups attributed to the bound water molecules [24,25]. The adsorption band at 3396 cm^{-1} denotes the availability of the ammonium moiety band, implying the presence of CTAB in both *RSBE*$_m$ and *RSBE*$_m$@P. The adsorption bands at 2850–2929 cm^{-1} are related to C—H stretching vibrations; meanwhile, peaks at 1650 and 1450 cm^{-1} indicate both asymmetric and symmetric bending of N^+-CH3 [19]. The N—H bend (1550 cm^{-1}) is evident in *RSBE*$_m$, confirming the presence of surfactant in the reactivated material. On *RSBE*$_m$@P and N-SBE@P, a peak extension at 1300 cm^{-1} indicates a P=O group after phosphate adsorption [26]. Meanwhile, the prominent peak at 1050 cm^{-1} corresponds to the Si—O group, bending from the tetrahedral surface. The bromide band, originating from the intercalated surfactant, is present in both *RSBE*$_m$ and *RSBE*$_m$@P at 720 cm^{-1}, while the peak at <590 cm^{-1} indicates Si-O-Al vibration [27].

The N_2 adsorption-desorption isotherm curves, as depicted in Fig. 4, along with the BET parameters outlined in Table 1, exhibit a consistent type IV N_2 sorption behavior across various sample variations. This type IV sorption pattern is typically associated with materials boasting a substantial specific surface area, akin to the findings in Sellaoui et al. (2018) [28], and is particularly well-suited for elucidating the structural features of substantial mesopores and macropores. For both *RSBE*$_m$ and N-SBE, the noteworthy volume of N_2 adsorbed at relatively low pressure (*P*/*Po*) suggests that N_2 molecules primarily engage with the material surface through van der Waals forces [29]. Furthermore, the appearance of plateaus at higher relative pressures indicates a saturation point, where N_2 molecules no longer interact with the material surface but

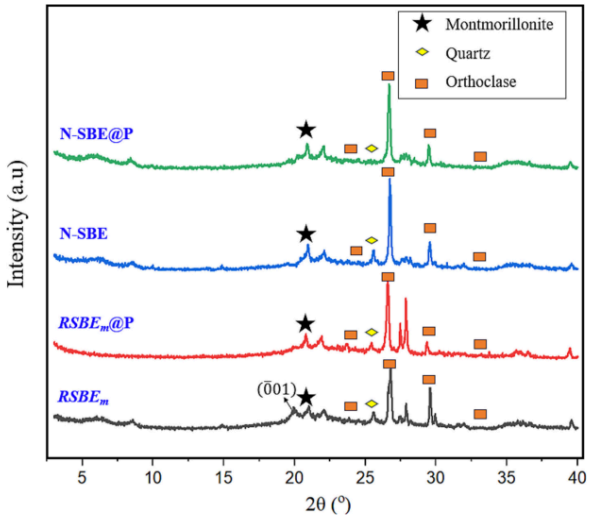

Fig. 2. The X-ray diffraction patterns of *RSBE*$_m$, *RSBE*$_m$@P, N-SBE, and N-SBE@P.

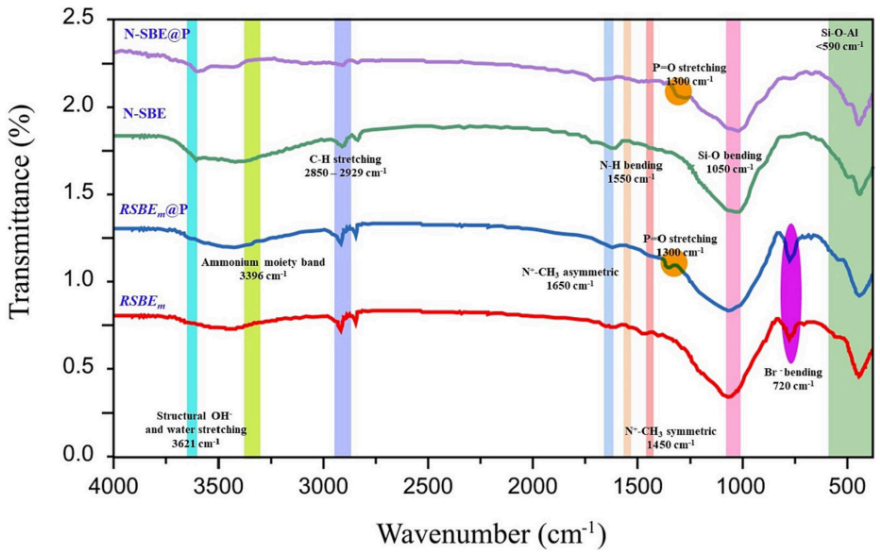

Fig. 3. FTIR spectra of *RSBE*$_m$, *RSBE*$_m$@P, N-SBE, and N-SBE@P.

instead occupy the internal pores of the material. In terms of hysteresis loops, all adsorbents exhibit a consistent H3-type pattern. Hysteresis loops of the H3 type are characterized by the presence of irregular pores or structures, often associated with slit shape [30]. Table 1 provides quantitative insights, revealing that the monolayer volume (V_m) of N_2 adsorbed on *RSBE*$_m$ surpasses that of N-SBE, with values of 13.60 cm^3/g and 11.04 cm^3/g, respectively. Furthermore, the specific surface area of *RSBE*$_m$ (59.25 m^2/g) outpaces that of N-SBE (48.12 m^2/g). These findings collectively indicate an enhancement in the textural characteristics of *RSBE*$_m$, attributable to the intercalation of surfactants.

The morphological structures of *RSBE*$_m$, *RSBE*$_m$@P, N-SBE, and N-SBE@P are presented in Fig. 5. According to the analysis, *RSBE*$_m$ exhibits high heterogeneity, the most favorable adsorbent for phosphate adsorption. *RSBE*$_m$@P has pores of a similar size to *RSBE*$_m$ but with a somewhat more even distribution, indicating phosphate ion attachment in a less randomly nature. In contrast, N-SBE has high homogeneity but limited surface area for phosphate ion attachment due to its tight spacing. The dimensions of the *RSBE*$_m$, *RSBE*$_m$@P, N-SBE, and N-SBE@P are measured using Image J software (the calculated data are presented in Table S4 – S7) and found at ca. 4.9 μm. Meanwhile, their elements are analyzed using EDS. Table 2 shows the presence of the P element in *RSBE*$_m$@P is 0.29 %; however, no P element is detected in N-SBE@P. A possible explanation is the uneven attachment of phosphate on the material's surface. A study conducted by Xing et al. (2020) mentioned that the absence of P element in natural clays after phosphate adsorption indicates that there is no significant binding or attachment of phosphate ions to the clay materials [31]. This absence of detection implies that the natural clays, including N-SBE, did not effectively retain or interact with phosphate ions during the adsorption process. Meanwhile, the mapping of the significant consisting elements shows that they are uniformly spread across the surface.

The influence of pH value is one of the most critical parameters in adsorption, notably in controlling the dominant phosphate species and ζ-potential. pH value correlates to the degree of ionization and surface charge of the adsorbate-adsorbent, allowing distinct charges to generate a diverse adsorption efficiency. Fig. 6(a) presents the ζ-potential evaluation of *RSBE*$_m$ and N-SBE, where both materials result in pH$_{pzc}$ of 7.2. The distribution fraction of phosphate forms, such as H_3PO_4, $H_2PO_4^-$, HPO_4^{2-}, and PO_4^{3-}, in an aqueous medium is also summarized in Fig. 6(b). These results imply that at the working pH value (pH = 7), the interaction between the adsorbent and adsorbate is electrostatically driven, as both *RSBE*$_m$ and N-SBE are positively charged, while the prevalent phosphate forms at the designated pH value are the negative $H_2PO_4^-$ and HPO_4^{2-}.

3.3. The influence of initial phosphate concentration on the performance of *RSBE*$_m$

Fig. 7a-b depict the overall declining removal rate of phosphate using *RSBE*$_m$ and N-SBE as C_o increases. The significant difference between the high concentration and the limited availability of active sites leads to a reduction in the portion of phosphate molecules that can bind to the surface of *RSBE*$_m$. Both figures reveal that the adsorption of phosphate reaches the highest removal rate (97.7 % for *RSBE*$_m$ and 39.76 % for N-SBE) at C_o = 150 mg/L. The rate is then reduced to 91.8 % and 31.71 % for *RSBE*$_m$ and N-SBE, respectively, when C_o is raised to 250 mg/L. This indicates that all sites of *RSBE*$_m$ and N-SBE have been already saturated with phosphate, leading to competition among phosphate molecules for the remaining active sites of *RSBE*$_m$ and N-SBE, resulting in decreased adsorptive capacity.

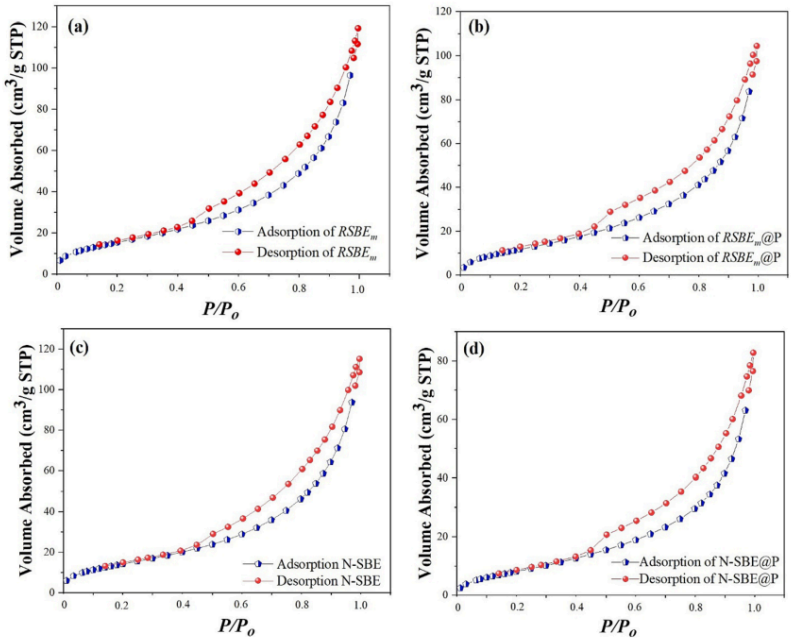

Fig. 4. N_2 adsorption-desorption isotherms of (a) $RSBE_m$, (b) $RSBE_m$@P, (c) N-SBE, and (d) N-SBE@P.

Table 1
The textural properties of $RSBE_m$, $RSBE_m$@P,N-SBE, and N-SBE@P.

	$RSBE_m$	$RSBE_m$@P	N-SBE	N-SBE@P
Monolayer volume (V_m, cm^3/g, STP)	13.60	12.56	11.04	7.84
BET surface area (S_{BET}, m^2/g)	59.25	54.71	48.12	34.16
Pore volume (V_p, cm^3/g)	0.16	0.15	0.14	0.10

3.4. The isotherm and thermodynamic studies of phosphate adsorption using $RSBE_m$

To evaluate the phosphate adsorption behavior on $RSBE_m$, the adsorption data at equilibrium are fitted into five isotherm models, e.g., Langmuir, Freundlich, Sips, Redlich-Peterson, and Temkin. The developed graphs are presented in Fig. 8, while the computed parameters and constants are summarized in Table 3. According to Giles classification [30], the isotherm profile at all temperature levels (Fig. 8) exhibits an L-behavior, which proves that $RSBE_m$ has a high affinity for phosphate. The steep increase (as seen in the red boxes of Fig. 8) in the adsorption capacity at reduced concentration denotes the presence of more active sites in $RSBE_m$, triggering the phosphate adsorption onto its surface. Sequentially, further increasing the concentration makes it more challenging for phosphate molecules to occupy the voids due to the formation of a monolayer on the surface of the binding sites [32].

A careful comparison of phosphate adsorption on $RSBE_m$ shows that the equilibrium data matches the Langmuir model, as indicated by their higher R^2_{adj} values. Fig. 8 also suggests that the model shares similar predicted q_e values as the experimental ones, confirming the validity of the Langmuir model to illustrate the phosphate adsorption onto $RSBE_m$. Further, this result is supported by (1) the heterogeneity factors of both Sips (n_s) and Redlich-Peterson (β) for $RSBE_m$, which is close to unity, and (2) the non-zero value of K_s; the two justifications inferred that this adsorption mechanism is leaning towards Langmuir. The data conformity to the Langmuir isotherm reveals the tendency of the adsorbate to form a monolayer on the $RSBE_m$ surface and that the adsorption happens at the particular homogeneous sites of $RSBE_m$ [35].

The increasing values of the Langmuir constant (K_L) from 0.09 to 0.13 L/mg as the temperature increases from $T = 30$ °C to $T = 50$ °C shows that the adsorption favors a higher temperature and signifies the endothermic behavior of the phosphate adsorption process. The computed $q_{m(L)}$ is being monitored to escalate from 101.6 mg/g at $T = 30$ °C to 178.8 mg/g at $T = 50$ °C. Solute molecules tend to have elevated kinetic energy at higher temperatures, increasing the randomness of the molecules. As a result of the high mobility of the solute molecules, the interaction between the solute and the adsorbent surface is accelerated.

The favorability of phosphate adsorption onto the $RSBE_m$ surface is verified using 1/n and R_L constants from the Freundlich and Langmuir models. Table 2 shows that all $1/n$ and R_L values at various temperature levels range between 0 and 1, validating the favorable nature of the adsorption [33]. The Temkin model is applicable to assess the adsorption energy, as one of its constants, b_T, is related to the heat of adsorption (E, kJ/mol). The obtained E indicates whether the process runs by physisorption ($E < 1$ kJ/mol), chemisorption ($E > 20$ kJ/mol), or both

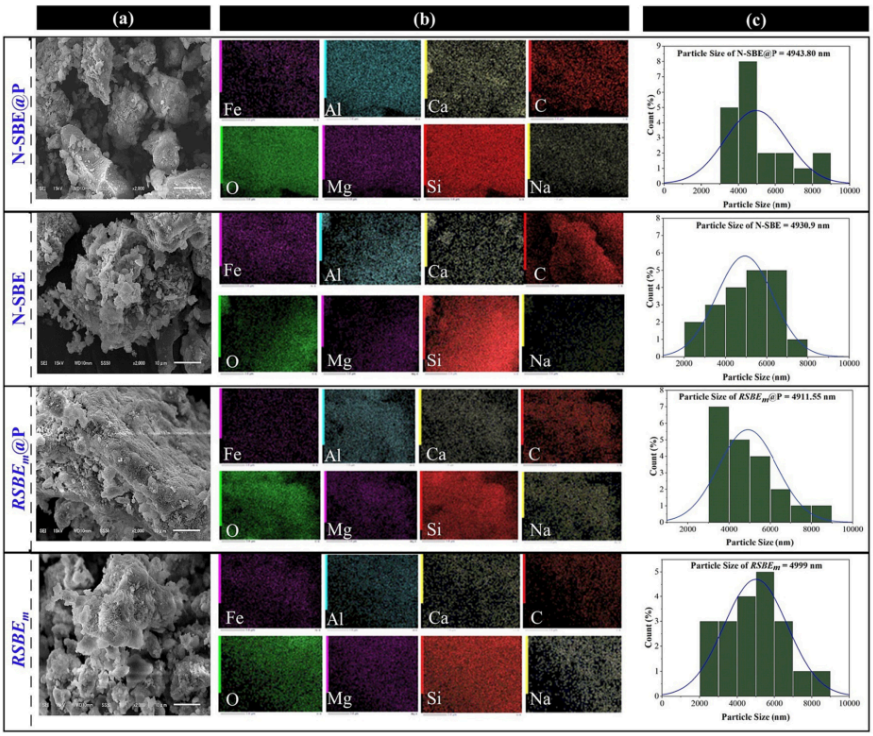

Fig. 5. (a) SEM images (magnified 2000 times with gold coating), (b) EDS mapping, and (c) particle size histogram (analyzed using ImageJ software) of *RSBE*$_m$, *RSBE*$_m$@P, N-SBE, and N-SBE@P. (For interpretation of the references to colour in this figure legend, the reader is referred to the web version of this article.)

Table 2
EDS analysis of *RSBE*$_m$, *RSBE*$_m$@P, N-SBE, and N-SBE@P.

Elements	Atom percentage (%)			
	RSBE$_m$	*RSBE*$_m$@P	N-SBE	N-SBE@P
C	12.49	19.33	18.70	23.73
O	56.14	46.40	54.99	43.10
Na	0.24	–	–	0.40
Mg	3.94	3.44	3.19	5.80
Al	5.73	5.60	3.24	3.39
Si	19.92	19.80	15.65	16.84
P	–	0.29	–	–
Ca	0.32	0.76	0.76	0.59
Fe	0.93	4.38	3.48	6.16
Total	100	100	100	100

($1 < E < 20$ kJ/mol) [36]. As seen in Table 3, all E values are <1 kJ/mol, indicating that physical interaction drives adsorption [37].

The calculated thermodynamic parameters are listed in Table 4, where negative results of ΔG° at variations of $T = 30$ °C, 40 °C, and 50 °C emphasize the feasibility and spontaneous occurrence of the adsorption process. The ΔH° value is obtained at 14.89 kJ/mol; this indicates the phosphate adsorption process is endothermic. The positive ΔS° supports the endothermic nature of phosphate adsorption since higher temperature allows the solid-liquid interface to possess more randomness, leading to a greater attraction between phosphate molecules and *RSBE*$_m$.

3.5. Adsorption kinetic study

Fig. 9 portrays the kinetic profile of phosphate adsorption using *RSBE*$_m$ at three temperature (T) levels, while the fitted parameters using several kinetic models are outlined in Table 5. As seen from the figure, a notable increase in q_t is observed in the first 60 mins, continued by the gradual increment until it reaches the equilibrium at $t_{eq} = 150$ min. Table 5 presents the kinetic parameters of the phosphate adsorption process using *RSBE*$_m$. Of the three adsorption kinetics models, the correspondence of the adsorption rate could be carried out by comparing q_{exp} (experimental adsorption capacity) and q_e (predicted adsorption capacity) values for each kinetic model. The computed q_e for PFO and PSO models exhibits that the first may better represent the experimental data than the latter, indicating that physical interaction between *RSBE*$_m$ and phosphate molecules best governs the adsorption. PFO also defines

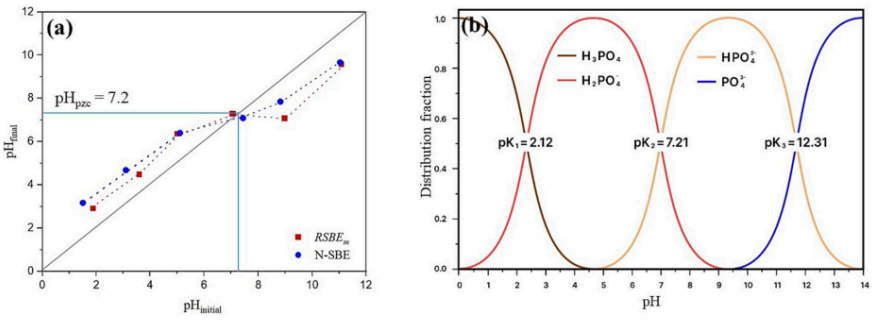

Fig. 6. (a) The pH_{pzc} analysis of $RSBE_m$ and N-SBE, (b) the phosphate distribution fraction.

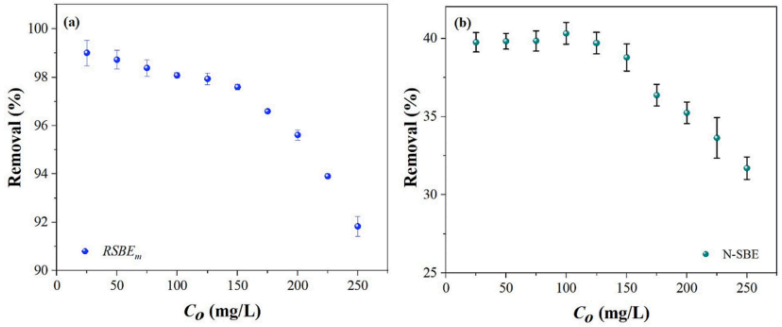

Fig. 7. The influence of initial phosphate concentration on the phosphate removal using (a) $RSBE_m$ and (b)N-SBE (Adsorbent loading = 0.1 wt%, pH = 7, t = 150 min, T = 30 °C).

the possibility that surface response is the mechanism that regulates the adsorption rate [38], suggesting that the surface-active sites and affinity may be the limiting factors for phosphate adsorption on $RSBE_m$. The value of k_1 is greater than k_2, implying that the rate-limiting phase in the phosphate adsorption onto $RSBE_m$ is physical diffusion within particles [39]. However, as frequently accepted, the kinetic adsorption results may also provide a different interpretation of the mechanism controlling the adsorption rate. Based on the fitted adsorption kinetic graphs, the R^2_{adj} value of PSO is slightly higher than PFO, showing that the mechanism controlling phosphate adsorption on $RSBE_m$ involves the chemical interaction – which in this case, is driven by the ion exchange or electron transfer between the adsorbent and adsorbate. Furthermore, the adsorption rate constants (k_1 and k_2) tend to rise with increasing temperature, emphasizing the endothermic nature of the phosphate adsorption process. This is supported by the observed adsorption rate (α) from the Elovich model. As seen, the α value enhances from 11.5 mg/g.min at T = 30 °C to 13.2 mg/g.min at T = 50 °C. Meanwhile, the desorption constant (β) value is primarily independent of T within the tested levels, signifying the stability of the binding between phosphate molecules onto the active sites of $RSBE_m$ [40].

To evaluate the mass transfer in adsorption kinetics, the kinetics data are further fitted to the IPD model, as this model can also be applied to elaborate the stepwise mechanism of phosphate removal in the examined system. As seen in Fig. 10, the system has two linear segments, with the summarized IPD parameter values provided in Table 6. The first segment represents the fast surface adsorption of phosphate that happened in the outermost site of $RSBE_m$, substantiated and supported by high diffusion rate ($k_{IPD,1}$) values. The enormous initial unoccupied spaces of adsorbent and massive dissolved solute concentration on the adsorbent surface contribute to the increased mass transfer rate of phosphate from the bulk solution to the adsorbent surface. Following the first one, the second segment of intraparticle diffusion of phosphate towards smaller pores sees a lower constant rate value ($k_{IPD,2}$) compared with $k_{IPD,1}$. This happens because as the adsorption persists, bare binding sites in the adsorbent are gradually occupied with the molecular substance of the solute, establishing an interface between the solute and the solution. Subsequently, slower adsorption of the remaining solute may occur [34]. Another reason is the enlarged boundary layer in the second segment, as implied by the higher C_2 value (boundary layer in the second segment) compared with C_1 (boundary layer in the first segment). This heightened boundary layer increases the energy barrier close to the interface and, as a result, decelerates the diffusion process of phosphate to $RSBE_m$ [41].

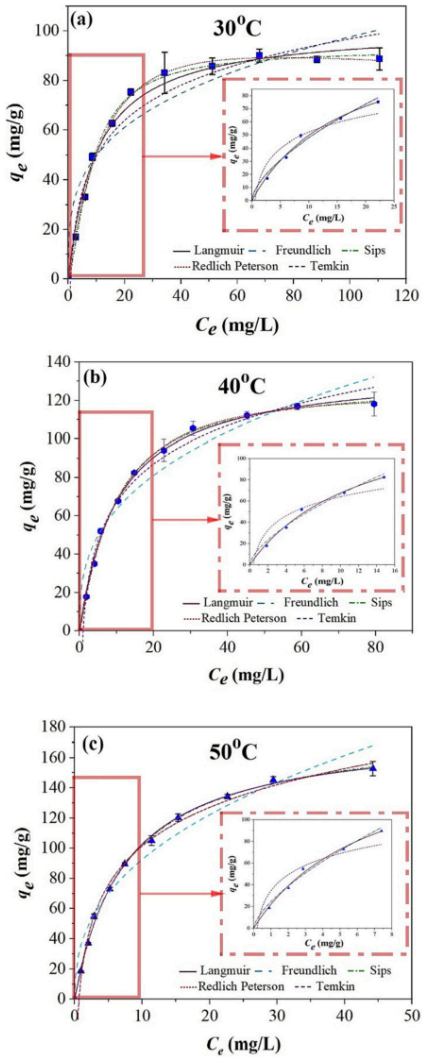

Fig. 8. The equilibrium adsorption data of the phosphate removal using $RSBE_m$ at (a) T = 30 °C, (b) T = 40 °C, and (c) T = 50 °C, fitted to several models (adsorption condition: $RSBE_m$ loading = 0.1 wt%, t = 150 min, pH = 7).

Table 3
The fitted isotherm parameters for the phosphate adsorption onto $RSBE_m$.

Model	Parameter	$RSBE_m$		
		30 °C	40 °C	50 °C
Langmuir	$q_{m(L)}$ (mg/g)	101.6 ± 3.0	136.9 ± 2.4	178.8 ± 0.1
	K_L (L/mg)	0.09 ± 0.01	0.10 ± 0.01	0.13± 0.01
	R_L [a]	0.129	0.120	0.095
	R^2	0.9878	0.9967	0.9988
	R^2_{adj}	0.9850	0.9964	0.9980
Freundlich	K_f ((mg/g)(L/mg)$^{1/n}$)	25.5 ± 5.0	28.1 ± 4.4	36.8 ± 4.1
	$1/n$	0.291	0.354	0.400
	R^2	0.9905	0.9491	0.9710
	R^2_{adj}	0.8992	0.9397	0.9640
Sips	$Q_{m(S)}$ (mg/g)	92.6 ± 1.7	129.7 ± 3.1	212.5 ± 0.1
	K_s (L/mg)	0.05 ± 0.01	0.08 ± 0.01	0.13 ± 0.01
	n_s	0.998	0.997	0.962
	R^2	0.9977	0.9991	0.9990
	R^2_{adj}	0.9960	0.9979	0.9984
Redlich-Peterson	K_R (L/mg)	7.44 ± 0.49	11.67 ± 0.76	14.85 ± 0.74
	a_R ((L/mg)$^{\beta}$)	0.03 ± 0.01	0.06 ± 0.01	0.007 ± 0.002
	β	1.03± 0.04	1.05±0.09	1.04 ±0.05
	R^2	0.9988	0.9991	0.9990
	R^2_{adj}	0.9969	0.9976	0.9986
Temkin	A_T (L/mg)	1.13 ± 0.35	1.02 ± 0.1	1.5 ± 0.119
	b_T (J/mol)	123.2 ± 3.2	90.4 ±3.8	72.7 ± 2.0
	E (kJ/mol) [b]	0.020	0.021	0.022
	R^2	0.9600	0.9901	0.9955
	R^2_{adj}	0.9568	0.9884	0.9941

[a] R_L = separation factor. $R_L = \frac{1}{(1 + bC_0)}$; adsorption process is categorized as: favorable if $0 < R_L < 1$, unfavorable if $R_L > 1$, linear is $R_L = 1$, and irreversible if $R_L = 0$ [33].

[b] E = Constant related to the heat of adsorption (kJ/mol). $E = \frac{RT}{b_T}$ [34].

Table 4
Thermodynamic parameters of phosphate adsorption onto $RSBE_m$.

T	$\Delta G°$ (kJ/mol)	$\Delta H°$ (kJ/mol)	$\Delta S°$ (KJ/mol.K)
30 °C	−23.6449	14.89	0.127
40 °C	−24.9166		
50 °C	−26.1883		

3.6. Reusability

The potential of $RSBE_m$ to be reused in six consecutive cycles is studied, and the result is presented in Fig. 11. In general, as the regeneration cycle intensifies, the phosphate adsorption capacity and removal efficiency of $RSBE_m$ deteriorate. After the first cycle, the removal efficiency is downgraded from 97.7 wt% to 88.2 wt%. The adsorption efficiency is maintained above 80 wt% until the fourth cycle before significantly decreasing to 69.5 wt% in the fifth cycle. The declining performance of $RSBE_m$ after reuse is mainly because of the intense interaction between phosphate molecules and the binding sites of $RSBE_m$, suggesting the presence of physisorption. This induces surface deactivation of the adsorbent, preventing subsequent phosphate adsorption [42,43]. A comparison to the other research in Table 7 shows that the pillared structure of layered $RSBE_m$ is relatively stable during adsorption.

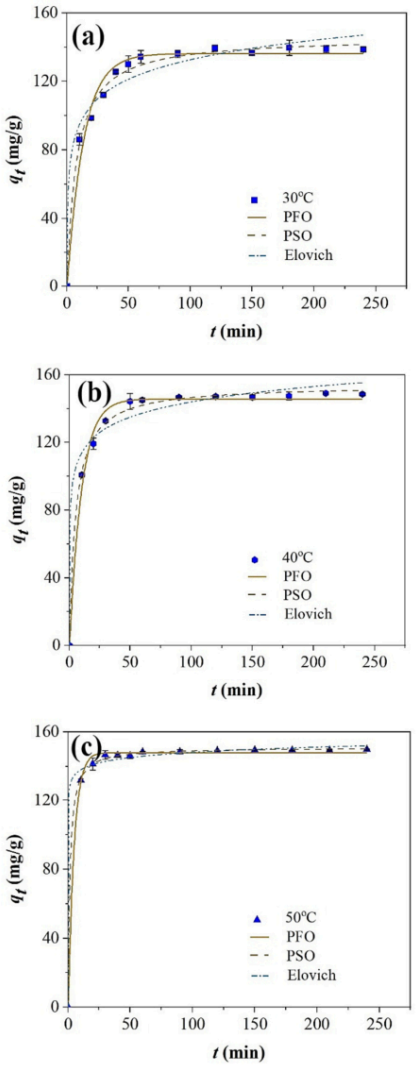

Fig. 9. The kinetic profile of phosphate adsorption onto $RSBE_m$ at (a) $T = 30$ °C, (b) $T = 40$ °C, and (c) $T = 50$ °C ($RSBE_m$ loading = 0.1 wt%, $C_o = 150$ mg/L, pH = 7).

Table 5
The fitted kinetic parameters of phosphate adsorption onto $RSBE_m$ at various temperatures.

Model	Parameter	$RSBE_m$		
		30 °C	40 °C	50 °C
	$q_{e,exp}$	135.0	145.8	146.3
Pseudo-first-order	q_{e1} (mg/g)	136.3	145.8	148.0
	k_1 (1/min)	0.074	0.101	0.215
	R^2	0.9799	0.9901	0.9980
	R^2_{adj}	0.9756	0.9896	0.9979
Pseudo-second-order	q_{e2} (mg/g)	145.9	151.0	153.9
	k_2 (g/mg.min)	0.001	0.001	0.005
	R^2	0.9922	0.9988	0.9999
	R^2_{adj}	0.9915	0.9961	0.9995
Elovich	α (mg/g.min)	11.5	12.5	13.2
	β (mg/g)	0.008	0.006	0.005
	R^2	0.9877	0.9900	0.9992
	R^2_{adj}	0.9861	0.9810	0.9990

3.7. Selectivity study of $RSBE_m$ towards phosphate using the single compound and binary systems approach

In industrial-scale wastewater treatment processes, the occurrence of waste phosphates in single chemical forms is uncommon; they typically manifest as a blend of multiple pollutants. Therefore, single-compound, such as $H_2PO_4^-/HPO_4^{2-}$,NO_3^-, SO_4^{2-}, CO_3^{2-}, and Cl^- are used to determine the selectivity of $RSBE_m$ towards phosphate ions. Fig. 12 illustrates the experimental adsorption isotherms in single-compound of NO_3^-, SO_4^{2-}, CO_3^{2-}, and Cl^- on $RSBE_m$ at various temperatures in a single solution. Details of numbering pollutants to predict adsorption capacity on Table S8. The presence of Cl^- ions impose the most impact on the phosphate adsorption, reducing the capacity adsorption rate from 194.6 mg/g to 48.50 mg/g; then, followed by SO_4^{2-}, CO_3^{2-}, NO_3^- ions. This result is in accordance with the Helfferich electroselectivity theory, which mentions that most adsorbent prefers to adsorb ions of larger valency instead of lower valency [43]. The parameters of isotherms models for $H_2PO_4^-/HPO_4^{2-}$, NO_3^-, SO_4^{2-}, CO_3^{2-}, and Cl^- adsorption in single–compound system by $RSBE_m$ provided in Table S9. Furthermore, the presence of diverse chemical compounds in wastewater triggers competition among these compounds for adsorption onto adsorbent active sites. Therefore, comprehensive adsorption investigations involving multiple components become essential. In this particular study, the influence of ($H_2PO_4^-/HPO_4^{2-}$ on NO_3^-), ($H_2PO_4^-/HPO_4^{2-}$ on SO_4^{2-}), ($H_2PO_4^-/HPO_4^{2-}$ on CO_3^{2-}), ($H_2PO_4^-/HPO_4^{2-}$ on Cl^-) and vice versa were also studied. Fig. 13 (a-h) displays the adsorption isotherms for various binary systems by $RSBE_m$ at different temperature conditions.

This section offers a quantitative analysis aimed at enhancing our understanding of ($H_2PO_4^-/HPO_4^{2-}$ on NO_3^-), ($H_2PO_4^-/HPO_4^{2-}$ on CO_3^{2-}), ($H_2PO_4^-/HPO_4^{2-}$ on SO_4^{2-}), ($H_2PO_4^-/HPO_4^{2-}$ on Cl^-), (NO_3^- on $H_2PO_4^-/HPO_4^{2-}$), (CO_3^{2-} on $H_2PO_4^-/HPO_4^{2-}$), (SO_4^{2-} on $H_2PO_4^-/HPO_4^{2-}$), (Cl^- on $H_2PO_4^-/HPO_4^{2-}$) binary adsorption. As the Langmuir equation effectively describes the adsorption isotherms for $RSBE_m$, the extended Langmuir equation is applied to create an adsorption isotherm equation for the binary adsorption of $RSBE_m$. The extended Langmuir equation for the binary system is delineated by the following equations:

$$q_{e,x} = \frac{q_{m,x} K_{L,x} C_{e,x}}{1 + K_{L,x} C_{e,x} + K_{L,y} C_{e,y}} \quad (4)$$

$$q_{e,y} = \frac{q_{m,y} K_{L,y} C_{e,y}}{1 + K_{L,x} C_{e,x} + K_{L,y} C_{e,y}} \quad (5)$$

The parameters for all extended equations are derived from single-component adsorption parameters, which are consolidated in Table S10.

To utilize the extended Langmuir equation for modeling experi-

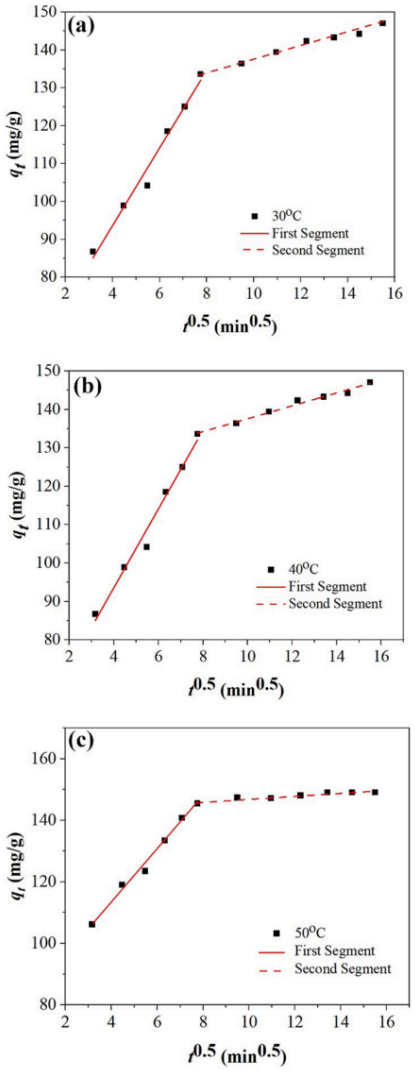

Fig. 10. The fitted kinetic data at (a) T = 30 °C, (b) T = 40 °C, and (c) T = 50 °C to the intraparticle diffusion model.

Table 6
The segmented kinetic parameter of phosphate adsorption onto $RSBE_m$, computed from the intraparticle diffusion model.

Intra-particle diffusion model	Parameter	$RSBE_m$		
		30 °C	40 °C	50 °C
First Segment	$k_{IPD,1}$ (mg/(g.min$^{0.5}$))	46.49	42.26	39.06
	C_1(mg/g)	1.20	26.61	35.68
	R^2	0.9661	0.9899	0.9887
	R^2_{adj}	0.9581	0.9815	0.9790
Second Segment	$k_{IPD,2}$ (mg/(g.min$^{0.5}$))	11.34	3.82	3.13
	C_2 (mg/g)	101.9	134.5	137.1
	R^2	0.9928	0.9012	0.9112
	R^2_{adj}	0.9837	0.8655	0.898
Without Segment	k_{IPD} (mg/(g.min$^{0.5}$))	27.37	19.85	18.53
	C (mg/g)	45.68	78.64	83.39
	R^2	0.9192	0.8092	0.8119
	R^2_{adj}	0.8925	0.7819	0.7860

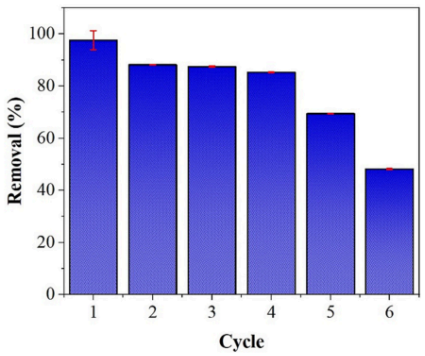

Fig. 11. The performance of $RSBE_m$ during its reusability study (adsorption condition: pH = 7, C_o = 150 mg/L, t = 150 min, T = 30 °C, $RSBE_m$ loading = 0.1 wt%).

mental data involving the binary adsorption of ($H_2PO_4^-$/HPO_4^{2-} on NO_3^-), ($H_2PO_4^-$/HPO_4^{2-} on SO_4^{2-}), ($H_2PO_4^-$/HPO_4^{2-} on CO_3^{2-}), ($H_2PO_4^-$/HPO_4^{2-} on Cl^-), (NO_3^- on $H_2PO_4^-$/HPO_4^{2-}), (SO_4^{2-} on $H_2PO_4^-$/HPO_4^{2-}), (CO_3^{2-} on $H_2PO_4^-$/HPO_4^{2-}), (Cl^- on $H_2PO_4^-$/HPO_4^{2-}), it is necessary to rely on the Langmuir equation parameters obtained from single-component adsorption. The main challenge lies in the accuracy of the equation itself when directly applied to binary adsorption data without any modification. In this research, all the Langmuir parameters for single-components exhibit strong correlation coefficients. However, when integrated into the extended Langmuir equation to represent the binary adsorption of ($H_2PO_4^-$/HPO_4^{2-} on NO_3^-), ($H_2PO_4^-$/HPO_4^{2-} on SO_4^{2-}), ($H_2PO_4^-$/HPO_4^{2-} on CO_3^{2-}), ($H_2PO_4^-$/HPO_4^{2-} on Cl^-), (NO_3^- on $H_2PO_4^-$/HPO_4^{2-}), (SO_4^{2-} on $H_2PO_4^-$/HPO_4^{2-}), (CO_3^{2-} on $H_2PO_4^-$/HPO_4^{2-}), (Cl^- on $H_2PO_4^-$/HPO_4^{2-}), they do not adequately capture the behavior of these two compounds in the system. In Fig. S1, Fig. S2, Fig. S3, and Fig. S4 the experimental adsorption isotherms for ($H_2PO_4^-$/HPO_4^{2-} and NO_3^-), ($H_2PO_4^-$/HPO_4^{2-} and SO_4^{2-}), ($H_2PO_4^-$/HPO_4^{2-} and CO_3^{2-}), ($H_2PO_4^-$/HPO_4^{2-} and Cl^-) in binary systems can be observed, along with the corresponding theoretical (three-dimensional) models that have been calcu-

Table 7
Reusability study of several adsorbents in the removal of phosphate.

Adsorbent	Adsorbate	Operating condition	Percent removal before and after 1st reuse	Ref
LPC@La(OH)$_3$	Phosphate	pH = 6; C_o = 10 mg/L; T = 25 °C	Before reuse = 99.5 wt% After 1st reuse = 93.5 wt%	[44]
Fe_3O_4@SiO_2@mLDH350	Phosphate	C_o = 200 g/L; T = 25 °C	Before reuse = 99.1 wt% After 1st reuse = 94 wt%	[45]
Fe(III)-complexed lignin	Phosphate	pH = 7; C_o = 5 g/L; T = 30 °C	Before reuse = 95.3 wt% After 1st reuse = 82.3 wt%	[46]
N_5-CB	Phosphate	pH = 3; C_o = 100 g/L; T = 25 °C	Before reuse = 86 wt% After 1st reuse = 70 wt%	[47]
Cerium hydroxide-encapsulated polystyrene D201 (HCO@201)	Phosphate	pH = 7.0 ± 0.1 C_o = 30 mg/L; T = 25 °C	Before reuse = 93 wt% After 1st reuse = 81.1 wt%	[48]
Zinc-Iron-Zirconium-coated Fe_3O_4/SiO_2	Phosphate	pH = 7.0; C_o = 10 mg/L; T = 25 °C	Before reuse = 85 wt% After 1st reuse = 70 wt%	[49]
Iron(III)–copper(II) binary oxides	Phosphate	pH = 7.0 ± 0.1 C_o = 200 mg/L; T = 25 °C	Before reuse = 95 wt% After 1st reuse = 84.74 wt%	[50]
Iron oxides	Phosphate	pH = 7.0 ± 0.1 C_o = 200 mg/L;	Before reuse = 89 wt% After 1st reuse = 82 wt%	[51]
La(OH)$_3$-modified $CoFe_2O_4$	Phosphate	pH = 7.8 C_o = 10 mg; T = 25 °C	Before reuse = 97.6 wt% After 1st reuse = 85.14 wt%	[52]
NaLa(CO$_3$)$_2$-coated magnetic biochar	Phosphate	pH = 7.0 C_o = 50 mg; T = 25 °C	Before reuse = 91 wt% After 1st reuse = 88 wt%	[53]
RSBE$_m$	Phosphate	pH = 7; C_o = 150 mg/L; T = 30 °C	Before reuse = 97.7 wt% After 1st reuse = 88.2 wt%	This study

LPC@La(OH)$_3$ = lanthanum hydroxide nanorods within lignin-derived porous carbon, Fe_3O_4@SiO_2@mLDH350 = synthesized a Fe_3O_4 core with a mesoporous SiO_2 shell nanocomposite and LDH layer by calcination 350 °C, N_5-CB = nitrogen (N)-doped Fe-rich biochar, La(OH)$_3$-modified $CoFe_2O_4$ = La(OH)$_3$-modified magnetic cobalt ferrite ($CoFe_2O_4$).

lated using the extended Langmuir modification.

The presence of competitive interactions among adsorbates exerts a noticeable influence on the adsorption affinities of individual components within a given system. In the context of an adsorption system, the presence of other components weakens the adsorption affinity that each component has for the adsorbent. Drawing upon the outcomes of the compatibility analysis conducted on single-component adsorption isotherm equations, as expounded upon in the preceding subsection, it becomes evident that the Langmuir isotherm equation stands out as the most apt choice for effectively characterizing the adsorption isotherms of $H_2PO_4^-$/HPO_4^{2-} ,NO_3^-, SO_4^{2-}, CO_3^{2-}, and Cl^- within single-component systems.

Henceforth, modifications are performed only to the Langmuir equation. In the context of a binary system characterized by competitive interactions among adsorbate molecules, the K_L parameter, linked to the affinity constant, can be mathematically expressed through the following equations:

$$K_{L,x\ bin} = K_{L,x}\left(1 - exp\left(-A_{xy}\right)\right) \tag{6}$$

$$K_{L,y\ bin} = K_{L,y}\left(1 - exp\left(-A_{yx}\right)\right) \tag{7}$$

Parameters A_{xy} and A_{yx} serve as correction factors that account for the influence of competition between adsorbate molecules (coded as in Table S8). By introducing the competition factor, Eqs. (6) and (7) can be reformulated as follows:

$$q_{e,x\,bin} = \frac{q_{m,x} K_{L,x}\ C_{e,x}}{1 + K_{L,x\ bin}\ C_{e,x} + K_{L,y\ bin}\ C_{e,y}} \tag{8}$$

$$q_{e,y\,bin} = \frac{q_{m,y} K_{L,y}\ C_{e,y}}{1 + K_{L,x\ bin}\ C_{e,x} + K_{L,y\ bin}\ C_{e,y}} \tag{9}$$

The values of parameters A_{xy} and A_{yx} were determined through simultaneous fitting of Eqs. (8) and (9) to the experimental binary adsorption data for ($H_2PO_4^-$/HPO_4^{2-} on NO_3^-), ($H_2PO_4^-$/HPO_4^{2-} on SO_4^{2-}), ($H_2PO_4^-$/HPO_4^{2-} on CO_3^{2-}), ($H_2PO_4^-$/HPO_4^{2-} on Cl^-). In Fig. S5, Fig. S6, Fig. S7, and Fig. S8, the experimental adsorption isotherms for ($H_2PO_4^-$/HPO_4^{2-} and NO_3^-), ($H_2PO_4^-$/HPO_4^{2-} and SO_4^{2-}), ($H_2PO_4^-$/HPO_4^{2-} and CO_3^{2-}), ($H_2PO_4^-$/HPO_4^{2-} and Cl^-) in binary systems can be monitored, along with the corresponding theoretical (three-dimensional) models that have been computed using the modified extended Langmuir modification. The models are implemented using Python with various packages, i.e., numpy, matplotlib, and mpl_tookits. The parameter values obtained for A_{12}, A_{21}, A_{13}, A_{31}, A_{14}, A_{41}, A_{15} and A_{51} are 0.464, 0.769, 0.464, 0.455, 0.464, 0.347, 0.464 and 0.296, respectively, with a regression coefficient (R^2) for each binary system of 0.998, 0.983, 0.994, 0.999. The modification of the Langmuir equation by incorporating a competition factor into the affinity coefficient successfully enhances the equation's capability to accurately represent the experimental data for binary adsorption.

In the context of binary system adsorption, a competitive ion arises among adsorbates as they vie for available adsorption sites on the surface of the adsorbent. While attractive forces operate not only between adsorbate and adsorbent but also among adsorbate molecules themselves, this intricate interplay can lead to a weakening of the interactions between adsorbates and the adsorbent material. Consequently, the K_L parameter value tends to decrease as a result of this competitive rivalry among adsorbate molecules. This particular aspect, which cannot be adequately captured by the original extended Langmuir equation, can be effectively addressed by introducing a competition factor to modify the K_L value. This modification empowers the extended Langmuir equation to accurately represent the binary adsorption data of $H_2PO_4^-$/HPO_4^{2-} , NO_3^-, SO_4^{2-}, CO_3^{2-}, and Cl^- on *RSBE$_m$*.

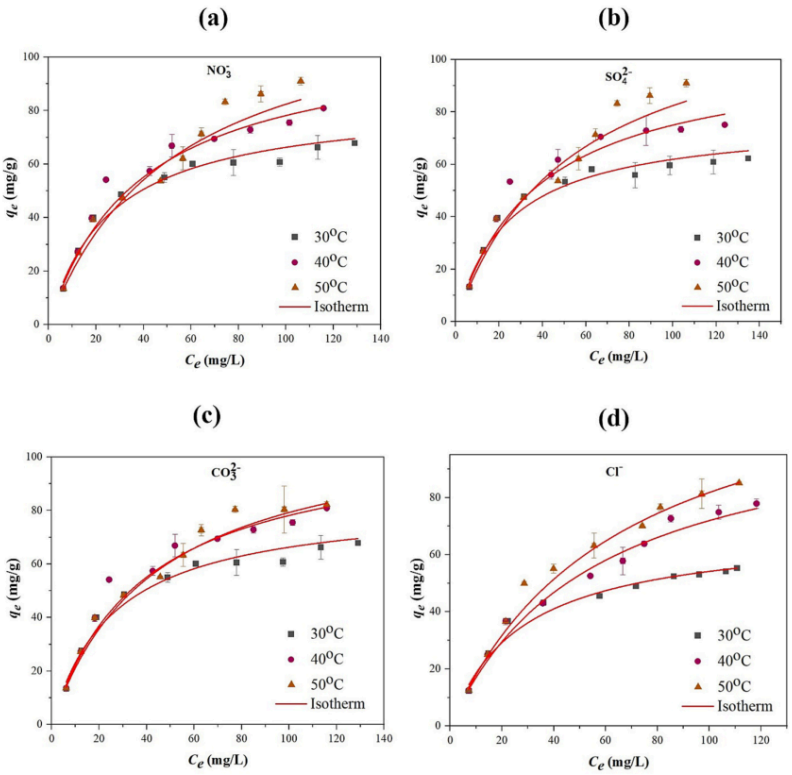

Fig. 12. The experimental adsorption isotherms in single-compound of NO_3^-, SO_4^{2-}, CO_3^{2-}, and Cl^- on *RSBE*$_m$.

3.8. Mechanism study

The intercalation mechanism of *RSBE*$_m$ can be illustrated in Fig. 14, while the interaction mechanism between phosphate and *RSBE*$_m$ is presented in Fig. 15 by incorporating data on the surface properties of *RSBE*$_m$ and its adsorption behavior. *RSBE*$_m$ is constituted by (1) the negatively charged SBE layers – one layer of SBE consists of two tetrahedral silica sheets and one octahedral aluminum sheet, and (2) the intercalated CTAB, where its cationic head attaches on the surface of the layer, and the tail acts like a pillar to expand the *d*-spacing of the adsorbent from 2.156 Å to 3.234 Å. This expanded adsorbent version may increase the phosphate molecule diffusion rate into *RSBE*$_m$.

Based on the adsorption behavior observed in this study, the removal of phosphate using *RSBE*$_m$ requires high temperature. Hydroxide ions (OH^-) from bound water play a role in hydrolyzing phosphate salts into phosphate ions. Phosphate ions are then adsorbed on the interlayer of *RSBE*$_m$ through electrostatic interactions between negatively charged phosphate ions and the positively charged interlayer of *RSBE*$_m$ at the working pH value (pH = 7), along with the ammonium groups from CTAB. The C—H and N^+-CH_3 groups from CTAB also contribute to increasing the interlayer area of *RSBE*$_m$, allowing more phosphate to be adsorbed. The P═O groups of phosphate play a role in stabilizing the adsorbed phosphate ions on the interlayer of *RSBE*$_m$, thus illustrating the adsorption mechanism of phosphate on *RSBE*$_m$ (Fig. 15) as follows: (1) rapid migration of phosphate molecules from the bulk solution to the *RSBE*$_m$ boundary layer, (2) gradual diffusion through the boundary layer to the *RSBE*$_m$ interlayer – this gradual diffusion process has been confirmed in N_2 sorption, where *RSBE*$_m$ porosity increases after surfactant intercalation, (3) electrostatic interaction between phosphate anions and the positively charged CTA^+ surface of *RSBE*$_m$. The presence of competing ions or binary adsorption can also interfere with phosphate adsorption by *RSBE*$_m$, however, the illustration regarding this aspect is not included.

4. Conclusions

RSBE$_m$ intercalated at the operating condition of r_{hex} = 1:5, m_c = 0.5 wt%, and T_i = 30 °C, is effectively used as an adsorbent for phosphate

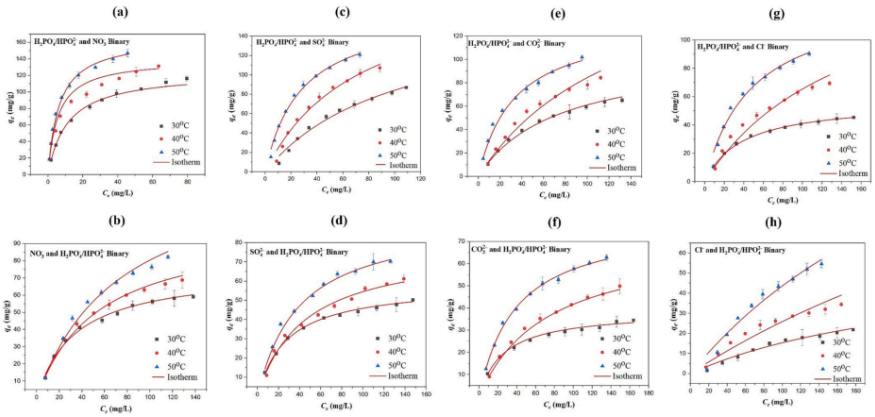

Fig. 13. Binary adsorption of (a) $H_2PO_4^-/HPO_4^{2-}$ in the presence of NO_3^-, (b) NO_3^- in the presence of $H_2PO_4^-/HPO_4^{2-}$, (c) $H_2PO_4^-/HPO_4^{2-}$ in the presence of SO_4^{2-}, (d) SO_4^{2-} in the presence of $H_2PO_4^-/HPO_4^{2-}$, (e) $H_2PO_4^-/HPO_4^{2-}$ in the presence of CO_3^{2-}, (f) CO_3^{2-} in the presence of $H_2PO_4^-/HPO_4^{2-}$, (g) $H_2PO_4^-/HPO_4^{2-}$ in the presence of Cl^-, and (h) Cl^- in the presence of $H_2PO_4^-/HPO_4^{2-}$ onto $RSBE_m$.

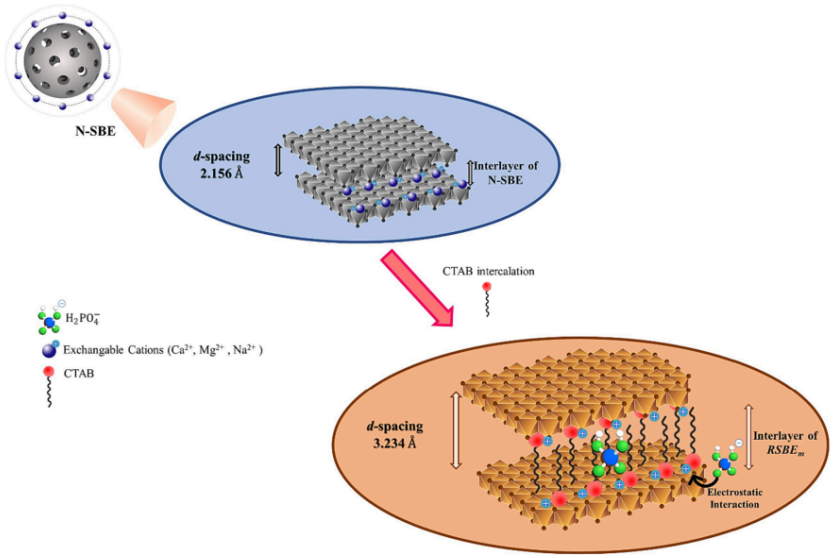

Fig. 14. Schematic illustration of the surfactant intercalation of $RSBE_m$.

removal from an aqueous solution. The phosphate removal rate using $RSBE_m$ is obtained at 97.7 wt% using the following condition: pH = 7, C_o = 150 mg/L, t = 150 min, T = 30 °C, $RSBE_m$ loading = 0.1 wt%. This indicates the strong affinity of $RSBE_m$ towards phosphate anions. Phosphate adsorption obeys the monolayer mechanism and is endothermic and spontaneous. The interaction between phosphate molecules and $RSBE_m$ is electrostatically-driven due to the opposite charges owned by the two. $RSBE_m$ shows excellent reusability, with the adsorption

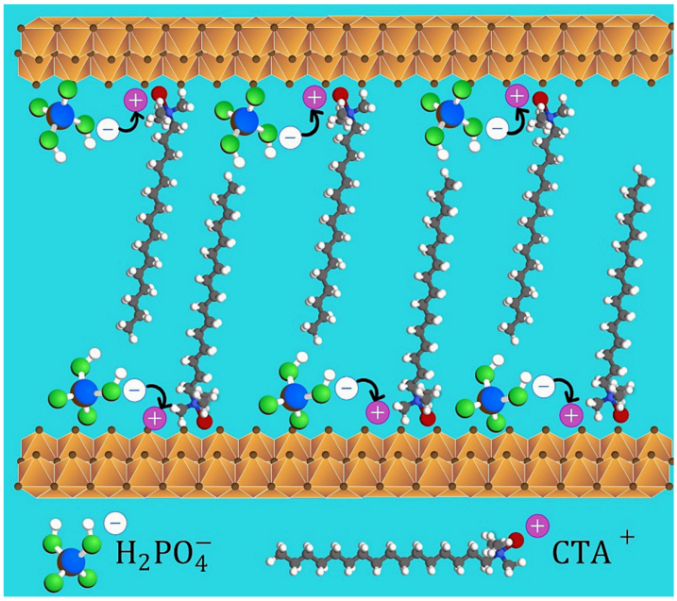

Fig. 15. The phosphate adsorption mechanism into the interlayer of $RSBE_m$.

capacity staying above 80 wt% for four cycles. The selectivity study towards phosphate ions in the presence of the co-existing anions also implies that this adsorbent has a good selectivity towards phosphate ions. Therefore, it can be concluded that $RSBE_m$ demonstrates great potential as a low-cost and sustainable substitute for commercial adsorbents in removing phosphate from water bodies.

CRediT authorship contribution statement

Putri Dwi Retno Asmoro: Writing – original draft, Visualization, Software, Methodology, Investigation, Conceptualization. **Maria Yuliana:** Writing – review & editing, Supervision, Resources, Project administration, Methodology, Funding acquisition, Conceptualization. **Felycia Edi Soetaredjo:** Supervision, Resources, Methodology, Data curation. **Suryadi Ismadji:** Supervision, Resources, Methodology, Funding acquisition, Conceptualization. **Masahiro Muraoka:** Supervision, Resources, Methodology. **Shintaro Kawano:** Supervision, Software, Investigation. **Motohiro Shizuma:** Supervision, Software, Investigation. **Grandprix Thomryes Marth Kadja:** Visualization, Software, Investigation. **Christian Julius Wijaya:** Validation. **Shella Permatasari Santoso:** Validation. **Ery Susiany Retnoningtyas:** Validation.

Declaration of competing interest

The authors declare that they have no known competing financial interests or personal relationships that could have appeared to influence the work reported in this paper.

Data availability

Data will be made available on request.

Acknowledgment

The authors thank the Osaka Institute of Technology, Osaka Research Institute of Industrial Science and Technology, and Institut Teknologi Bandung for providing the facilities for material characterizations. This project was supported by the Ministry of Education, Culture, Research, and Technology of the Republic of Indonesia and Widya Mandala Surabaya Catholic University through research grants no. 260C/WM01.5/N/2023, 7405/WM01/N/2022, and 3776/WM01/N/2023.

Appendix A. Supplementary data

Supplementary data to this article can be found online at https://doi.org/10.1016/j.jwpe.2024.104906.

References

[1] H.W. Paerl, T.G. Otten, R. Kudela, Mitigating the expansion of harmful algal blooms across the freshwater-to-marine continuum, Environ. Sci. Technol. 52 (2018) 5519–5529, https://doi.org/10.1021/acs.est.7b05950.
[2] M. Kuro-o, A phosphate-centric paradigm for pathophysiology and therapy of chronic kidney disease, Kidney Int. Suppl. 3 (2013) (2011) 420–426, https://doi.org/10.1038/kisup.2013.88.
[3] P. Loganathan, S. Vigneswaran, J. Kandasamy, N.S. Bolan, Removal and recovery of phosphate from water using sorption, Crit. Rev. Environ. Sci. Technol. 44 (2014) 847–907.

[4] H. Bacelo, Performance and prospects of different adsorbents for phosphorus uptake and recovery from water, Chem. Eng. J. 381 (2020), https://doi.org/10.1016/j.cej.2019.122566.

[5] A.E. Angkawijaya, S.P. Santoso, V. Bundjaja, F.E. Soetaredjo, C. Gunarto, A. Ayucitra, Y.H. Ju, A.W. Go, S. Ismadji, Studies on the performance of bentonite and its composite as phosphate adsorbent and phosphate supplementation for plant, J. Hazard. Mater. 399 (2020) 123130, https://doi.org/10.1016/j.jhazmat.2020.123130.

[6] B. Wang, H. Zhang, X. Hu, R. Chen, W. Guo, H. Wang, C. Wang, J. Yuan, L. Chen, S. Xia, Efficient phosphate elimination from aqueous media by La/Fe bimetallic modified bentonite: adsorption behavior and inner mechanism, Chemosphere 312 (2023) 137149, https://doi.org/10.1016/j.chemosphere.2022.137149.

[7] J. Fu, J.X. Yap, C.P. Leo, C.K. Chang, Carboxymethyl cellulose/sodium alginate beads incorporated with calcium carbonate nanoparticles and bentonite for phosphate recovery, Int. J. Biol. Macromol. 234 (2023) 123642, https://doi.org/10.1016/j.ijbiomac.2023.123642.

[8] Direktorat Jenderal Perkebunan, Produksi Kelapa Sawit Menurut Provinsi di Indonesia, 2017-2021, 2021 (2021) 2021.

[9] M.A. Sedghamiz, S. Raeissi, F. Attar, M. Salimi, K. Mehrabi, In-situ transesterification of residual vegetable oil in spent bleaching clay with alkali catalysts using CCD-RSM design of experiment, Fuel 237 (2019) 515–521, https://doi.org/10.1016/j.fuel.2018.09.116.

[10] N. Pourvosoughi, Polysel: an environmental-friendly CI engine fuel, Energy 111 (2016) 691–700, https://doi.org/10.1016/j.energy.2016.05.125.

[11] P. Subra-Paternault, C. Harscoat-Schiavo, R. Savoire, M. Brun, J. Velasco, V. Ruiz-Mendez, Utilization of pressurized CO2, pressurized ethanol and CO2-expanded ethanol mixtures for de-oiling spent bleaching earths, J. Supercrit. Fluids 149 (2019) 42–53, https://doi.org/10.1016/j.supflu.2019.03.016.

[12] S. Loh, Surface-active physicochemical characteristics of spent bleaching earth on soil-plant interaction and water-nutrient uptake: a review, Appl. Clay Sci. 140 (2017) 59–65, https://doi.org/10.1016/j.clay.2017.01.024.

[13] M. Yuliana, L. Trisna, F. Sari, V.B. Lunardi, Glycerol purification using reactivated spent bleaching earth from palm oil refineries: zero-waste approach, J. Environ. Chem. Eng. 9 (2021) 105239, https://doi.org/10.1016/j.jece.2021.105239.

[14] A. Merikhy, A. Heydari, H. Eskandari, F. Ghahraman-Rozegar, Carbonized spent bleaching earth as a low-cost adsorbent: a facile revalorization strategy via response surface methodology, Chemical Engineering and Processing-Process Intensification 158 (2020), https://doi.org/10.1016/j.cep.2020.108167.

[15] H. Bacelo, A.M.A. Pintor, S.C.R. Santos, R.A.R. Boaventura, C.M.S. Botelho, Performance and prospects of different adsorbents for phosphorus uptake and recovery from water, Chem. Eng. J. 381 (2020), https://doi.org/10.1016/j.cej.2019.122566.

[16] Y. Shao, J. Li, X. Fang, Z. Yang, Y. Qu, M. Yang, W. Tan, G. Li, H. Wang, Chemical modification of bamboo activated carbon surface and its adsorption property of simultaneous removal of phosphate and nitrate, Chemosphere 287 (2022) 132118, https://doi.org/10.1016/j.chemosphere.2021.132118.

[17] A. Khenifi, B. Zohra, B. Kahina, H. Houari, D. Zoubir, Removal of 2,4-DCP from wastewater by CTAB/bentonite using one-step and two-step methods: a comparative study, Chem. Eng. J. 146 (2009) 345–354, https://doi.org/10.1016/j.cej.2008.06.028.

[18] M.J. Rosen, Relationship of structure to properties in surfactants. III. Adsorption at the solid-liquid interface from aqueous solution, J. Am. Oil Chem. Soc. 52 (1975) 431–435, https://doi.org/10.1007/BF02637482.

[19] M. Yuliana, R.J. Sutrisno, S. Hermanto, S. Ismadji, C.J. Wijaya, S.P. Santoso, F. E. Soetaredjo, Y.H. Ju, Hydrophobic cetyltrimethylammonium bromide-pillared bentonite as an effective palm oil bleaching agent, ACS Omega (2020), https://doi.org/10.1021/acsomega.0c04238.

[20] A. Gürses, S. Karaca, M. Açikyildiz, M. Ejder, Thermodynamics and mechanism of cetyltrimethylammonium adsorption onto clayey soil from aqueous solutions, Chem. Eng. J. 147 (2009) 194–201.

[21] M. Mana, Regeneration of spent bleaching earth by treatment with cethyltrimethylammonium bromide for application in elimination of acid dye, Chem. Eng. J. 174 (2011) 275–280, https://doi.org/10.1016/j.cej.2011.09.026.

[22] D. Wan, Enhanced adsorption of aqueous tetracycline hydrochloride on renewable porous clay-carbon adsorbent derived from spent bleaching earth via pyrolysis, Langmuir 35 (2019) 3925–3936, https://doi.org/10.1021/acs.langmuir.8b04179.

[23] A. Kurniawan, H. Sutiono, Y.-H. Ju, F.E. Soetaredjo, A. Ayucitra, A. Yudha, S. Ismadji, Utilization of rarasaponin natural surfactant for organo-bentonite preparation: application for methylene blue removal from aqueous effluent, Microporous Mesoporous Mater. 142 (2011) 184–193, https://doi.org/10.1016/j.micromeso.2010.11.032.

[24] E.I. Unuabonah, F.O. Agunbiade, M.O. Alfred, T.A. Adewumi, C.P. Okoli, M. O. Omorogie, M.O. Akanbi, A.E. Ofomaja, A. Taubert, Facile synthesis of new amino-functionalized agrogenic hybrid composite clay adsorbents for phosphate capture and recovery from water, J. Clean. Prod. 164 (2017) 652–663, https://doi.org/10.1016/j.jclepro.2017.06.160.

[25] C. Topcu, B. Caglar, A. Onder, F. Coldur, S. Caglar, E.K. Guner, O. Cubuk, A. Tabak, Structural characterization of chitosan-smectite nanocomposite and its application in the development of a novel potentiometric monohydrogen phosphate-selective sensor, Mater. Res. Bull. 98 (2018) 288–299, https://doi.org/10.1016/j.materresbull.2017.09.068.

[26] Z. Wu, X. Yuan, H. Zhong, H. Wang, G. Zeng, X. Chen, H. Wang, L. Zhang, J. Shao, Enhanced adsorptive removal of p-nitrophenol from water by aluminum metal-organic framework/reduced graphene oxide composite, Sci. Rep. 6 (2016) 1–13, https://doi.org/10.1038/srep25638.

[27] N. Vanitha, T. Revathi, M. Sivasakthi, R. Jeyalakshmi, Microstructure properties of poly(phospho-siloxo) geopolymeric network with metakaolin as sole binder reinforced with n-SiO2 and n-Al2O3, J. Solid State Chem. 312 (2022), https://doi.org/10.1016/j.jssc.2022.123188.

[28] L. Sellaoui, F.E. Soetaredjo, S. Ismadji, A. Bonilla-Petriciolet, C. Belver, J. Bedia, A. Ben Lamine, A. Erto, Insights on the statistical physics modeling of the adsorption of Cd2+ and Pb2+ ions on bentonite-chitosan composite in single and binary systems, Chem. Eng. J. 354 (2018) 569–576, https://doi.org/10.1016/j.cej.2018.08.073.

[29] S. Brunauer, L.S. Deming, W.E. Deming, E. Teller, On a theory of the van der Waals adsorption of gases, J. Am. Chem. Soc. 62 (1940) 1723–1732, https://doi.org/10.1021/ja01864a025.

[30] C.H. Giles, T.H. MacEwan, S.N. Nakhwa, D. Smith, Studies in adsorption. Part XI.* A system, J. Chem. Soc. 846 (1960) 3973–3993.

[31] B. Xing, M. Ouyang, N. Graham, W. Yu, Enhancement of phosphate adsorption during mineral transformation of natural siderite induced by humic acid: mechanism and application, Chem. Eng. J. 393 (2020) 124730, https://doi.org/10.1016/j.cej.2020.124730.

[32] I. Langmuir, The adsorption of gases on plane surfaces of glass, mica and platinum, J. Am. Chem. Soc. 40 (1918) 1361–1403.

[33] T.W. Weber, R.K. Chakravorti, Pore and solid diffusion models for fixed-bed adsorbers, AICHE J. 20 (1974) 228–238, https://doi.org/10.1002/aic.690200204.

[34] S.P. Santoso, A.E. Angkawijaya, V. Bundjaja, A. Kurniawan, M. Yuliana, C.-W. Hsieh, A.W. Go, K.-C. Cheng, F.E. Soetaredjo, S. Ismadji, Investigation of the influence of crosslinking activation methods on the physicochemical and Cu(II) adsorption characteristics of cellulose hydrogels, J. Environ. Chem. Eng. 10 (2022) 106971, https://doi.org/10.1016/j.jece.2021.106971.

[35] L. Liu, X.-B. Luo, L. Ding, S.-L. Luo, Application of nanotechnology in the removal of heavy metal from water, in: Nanomaterials for the Removal of Pollutants and Resource Reutilization, Elsevier, 2019, pp. 83–147.

[36] M.A. Al-Ghouti, D.A. Da'ana, Guidelines for the use and interpretation of adsorption isotherm models: a review, J. Hazard. Mater. 393 (2020) 122383, https://doi.org/10.1016/j.jhazmat.2020.122383.

[37] U.A. Edet, A.O. Ifelebuegu, Kinetics, isotherms, and thermodynamic modeling of the adsorption of phosphates from model wastewater using recycled brick waste, Processes 8 (2020) 665.

[38] W. Rudzinski, W. Plazinski, Kinetics of solute adsorption at solid/solution interfaces: a theoretical development of the empirical pseudo-first and pseudo-second order kinetic rate equations, based on applying the statistical rate theory of interfacial transport, J. Phys. Chem. B 110 (2006) 16514–16525.

[39] L. Laysandra, F.H. Santosa, V. Austen, F.E. Soetaredjo, K. Foe, J.N. Putro, Y.-H. Ju, S. Ismadji, Rarasaponin-bentonite-activated biochar from durian shells composite for removal of crystal violet and Cr (VI) from aqueous solution, Environ. Sci. Pollut. Res. 25 (2018) 30680–30695.

[40] R.-L. Tseng, H.N. Tran, R.-S. Juang, Revisiting temperature effect on the kinetics of liquid–phase adsorption by the Elovich equation: a simple tool for checking data reliability, J. Taiwan Inst. Chem. Eng. 136 (2022) 104403, https://doi.org/10.1016/j.jtice.2022.104403.

[41] J.C. Igwe, C.O. Onyegbado, A.A. Abia, Studies on the kinetics and intraparticle diffusivities of BOD, colour and TSS reduction from palm oil mill effluent (POME) using boiler fly ash, Afr. J. Environ. Sci. Technol. 4 (2010).

[42] H. Xi, Q. Li, Y. Yang, J. Zhang, F. Guo, X. Wang, S. Xu, S. Ruan, Highly effective removal of phosphate from complex water environment with porous Zr-bentonite alginate hydrogel beads: facile synthesis and adsorption behavior study, Appl. Clay Sci. 201 (2021) 105919, https://doi.org/10.1016/j.clay.2020.105919.

[43] J. Wang, Y. Xia, Fe-substituted isoreticular metal-organic framework for efficient and rapid removal of phosphate, ACS Appl Nano Mater 2 (2019) 6492–6502, https://doi.org/10.1021/acsanm.9b01429.

[44] X. Liu, E. Zong, W. Hu, P. Song, J. Wang, Q. Liu, Z. Ma, S. Fu, Lignin-derived porous carbon loaded with La(OH) 3 nanorods for highly efficient removal of phosphate, ACS Sustain. Chem. Eng. 7 (2019) 758–768, https://doi.org/10.1021/acssuschemeng.8b04382.

[45] F. Li, J. Jin, Z. Shen, H. Ji, M. Yang, Y. Yin, Removal and recovery of phosphate and fluoride from water with reusable mesoporous Fe3O4@mSiO2@mLDH composites as sorbents, J. Hazard. Mater. 388 (2020) 121734, https://doi.org/10.1016/j.jhazmat.2019.121734.

[46] X. Luo, C. Liu, J. Yuan, X. Zhu, S. Liu, Interfacial solid-phase chemical modification with Mannich reaction and Fe(III) chelation for designing lignin-based spherical nanoparticle adsorbents for highly efficient removal of low concentration phosphate from water, ACS Sustain. Chem. Eng. 5 (2017) 6539–6547, https://doi.org/10.1021/acssuschemeng.7b00674.

[47] C. Zhang, Y. Dong, W. Liu, D. Yang, J. Liu, Y. Lu, H. Lin, Enhanced adsorption of phosphate from pickling wastewater by Fe-N co-pyrolysis biochar: performance, mechanism and reusability, Bioresour. Technol. 369 (2023), https://doi.org/10.1016/j.biortech.2022.128263.

[48] W. Yang, X. Shi, H. Dong, H. Tang, W. Chen, M. Wu, M. Hua, W. Zhang, Fabrication of a reusable polymer-based cerium hydroxide nanocomposite with high stability for preferable phosphate removal, Chem. Eng. J. 405 (2021), https://doi.org/10.1016/j.cej.2020.126649.

[49] A. Drenkova-Tuhtan, M. Schneider, M. Franzreb, C. Meyer, C. Gellermann, G. Sextl, K. Mandel, H. Steinmetz, Pilot-scale removal and recovery of dissolved phosphate from secondary wastewater effluents with reusable ZnFeZr adsorbent @ Fe3O4/SiO2 particles with magnetic harvesting, Water Res. 109 (2017) 77–87, https://doi.org/10.1016/j.watres.2016.11.039.

[50] G. Li, S. Gao, G. Zhang, X. Zhang, Enhanced adsorption of phosphate from aqueous solution by nanostructured iron(III)-copper(II) binary oxides, Chem. Eng. J. 235 (2014) 124–131, https://doi.org/10.1016/j.cej.2013.09.021.
[51] Z. Ajmal, A. Muhmood, M. Usman, S. Kizito, J. Lu, R. Dong, S. Wu, Phosphate removal from aqueous solution using iron oxides: adsorption, desorption and regeneration characteristics, J. Colloid Interface Sci. 528 (2018) 145–155, https://doi.org/10.1016/j.jcis.2018.05.084.
[52] Y. Chen, R. Xu, Y. Li, Y. Liu, Y. Wu, Y. Chen, J. Zhang, S. Chen, H. Yin, Z. Zeng, S. Wang, Z. Peng, La(OH)3-modified magnetic CoFe2O4 nanocomposites: a novel adsorbent with highly efficient activity and reusability for phosphate removal, Colloids Surf. A Physicochem. Eng. Asp. 599 (2020), https://doi.org/10.1016/j.colsurfa.2020.124870.
[53] J. Qu, M.S. Akindolie, Y. Feng, Z. Jiang, G. Zhang, Q. Jiang, F. Deng, B. Cao, Y. Zhang, One-pot hydrothermal synthesis of NaLa(CO3)2 decorated magnetic biochar for efficient phosphate removal from water: kinetics, isotherms, thermodynamics, mechanisms and reusability exploration, Chem. Eng. J. 394 (2020), https://doi.org/10.1016/j.cej.2020.124915.

Efficient and selective phosphate removal from wastewater using surface-modified spent bleaching earth from palm oil refineries: A zero-waste approach

ORIGINALITY REPORT

3%	2%	4%	2%
SIMILARITY INDEX	INTERNET SOURCES	PUBLICATIONS	STUDENT PAPERS

PRIMARY SOURCES

1	Submitted to University of St Andrews Student Paper	1%
2	www.ncbi.nlm.nih.gov Internet Source	1%
3	Noerma J. Azhari, Bahaul F. Al-Haq, A.C. S Axel, Muhammad A. Rifialdy et al. "Ethylene-to-Aromatics over Metal-Free Hierarchical MFI Zeolite: Boosting the BTX Yield", Results in Engineering, 2025 Publication	1%
4	Maria Yuliana, Revano J. Sutrisno, Stefanus Hermanto, Suryadi Ismadji et al. "Hydrophobic Cetyltrimethylammonium Bromide-Pillared Bentonite as an Effective Palm Oil Bleaching Agent", ACS Omega, 2020 Publication	1%

Exclude quotes	On	Exclude matches	< 1%
Exclude bibliography	On		

Efficient and selective phosphate removal from wastewater using surface-modified spent bleaching earth from palm oil refineries: A zero-waste approach

GRADEMARK REPORT

FINAL GRADE

/100

GENERAL COMMENTS

PAGE 1

PAGE 2

PAGE 3

PAGE 4

PAGE 5

PAGE 6

PAGE 7

PAGE 8

PAGE 9

PAGE 10

PAGE 11

PAGE 12

PAGE 13

PAGE 14

PAGE 15

PAGE 16

PAGE 17